Remote Sensing of Environment 145 (2014) 55–67

Contents lists available at ScienceDirect

Remote Sensing of Environment

journal homepage: www.elsevier.com/locate/rse

Generating daily land surface temperature at Landsat resolution by fusing Landsat and MODIS data

Qihao Weng [a,*], Peng Fu [a,1], Feng Gao [b]

[a] Center for Urban and Environmental Change, Department of Earth and Environmental Systems, Indiana State University, Terre Haute, IN 47809, USA
[b] USDA-ARS, Hydrology and Remote Sensing Laboratory, Beltsville, MD 20705, USA

ARTICLE INFO

Article history:
Received 6 September 2013
Received in revised form 2 February 2014
Accepted 4 February 2014
Available online xxxx

Keywords:
Data fusion
Thermal infrared data
Land surface temperature
Annual temperature cycle
Urban landscape heterogeneity
Thermal imagery sharpening

ABSTRACT

Land surface temperature (LST) is a crucial parameter in investigating environmental, ecological processes and climate change at various scales, and is also valuable in the studies of evapotranspiration, soil moisture conditions, surface energy balance, and urban heat islands. These studies require thermal infrared (TIR) images at both high temporal and spatial resolution to retrieve LST. However, currently, no single satellite sensors can deliver TIR data at both high temporal and spatial resolution. Thus, various algorithms/models have been developed to enhance the spatial or the temporal resolution of TIR data, but rare of those can enhance both spatial and temporal details. This paper presents a new data fusion algorithm for producing Landsat-like LST data by blending daily MODIS and periodic Landsat TM datasets. The original Spatial and Temporal Adaptive Reflectance Fusion Model (STARFM) was improved and modified for predicting thermal radiance and LST data by considering annual temperature cycle (ATC) and urban thermal landscape heterogeneity. The technique of linear spectral mixture analysis was employed to relate the Landsat radiance with the MODIS one, so that the temporal changes in radiance can be incorporated in the fusion model. This paper details the theoretical basis and the implementation procedures of the proposed data fusion algorithm, Spatio-temporal Adaptive Data Fusion Algorithm for Temperature mapping (SADFAT). A case study was conducted that predicted LSTs of five dates in 2005 from July to October in Los Angeles County, California. The results indicate that the prediction accuracy for the whole study area ranged from 1.3 K to 2 K. Like existing spatio-temporal data fusion models, the SADFAT method has a limitation in predicting LST changes that were not recorded in the MODIS and/or Landsat pixels due to the model assumption.

1. Introduction

Land surface temperature (LST), as frequently referred to as the skin temperature of the Earth's surface and as derived from remotely sensed thermal infrared (TIR) data, is a key parameter in analyzing and modeling the surface energy balance (Anderson et al., 2011; Trenberth, 1992), surface moisture and evapotranspiration (Carlson, 2007; Gillies, Carlson, Cui, Kustas, & Humes, 1997; Moran, 2004), and climate change of various spatial scales (Jin, Dickinson, & Zhang, 2005; Weng, 2009). LST and its spatial–temporal variations have long been foci of studies on surface Urban Heat Island (UHI) (Imhoff, Zhang, Wolfe, & Bounoua, 2010; Oke, 1982; Rajasekar & Weng, 2009; Streutker, 2003). Oke (1979) discriminated between the canopy layer UHI and the boundary layer UHI. The canopy layer UHI consists of air between the roughness elements, e.g., buildings and tree canopies, with an upper boundary just below roof level. Therefore, it relates closely to satellite-derived LST, although a precise transfer function between LST and the near ground air temperature is not yet available (Nichol, 1994). In addition, LST is useful for the examination of heat-related health issues and the vulnerability of human beings to heat stress (Harlan, Brazel, Prashad, Stefanov, & Larsen, 2006; Lafortezza, Carrus, Sanesi, & Davies, 2009), and the outbreak and propagation of vector-borne diseases (Liu & Weng, 2009; Reisen et al., 2004; Ruiz et al., 2010). Therefore, estimation of LST and assessing its variations are not only helpful to understand environmental and ecological processes, but also concerned with the well-being of humans.

Current satellite TIR data suitable for studying urban thermal environment or for solving urban environmental and health problems that are characterized by a high spatial variability – such as Landsat TM, ETM+, and ASTER – have a much coarser temporal resolution than it is needed. Given the long repeat cycle of these satellites, their TIR data are not suited for UHI monitoring. Surface UHI is not only a phenomenon of high spatial variability, but also of high temporal variability. For examining the health implications of UHI, such as heat-related epidemiological studies, routine LST estimation is essential (Liu & Weng, 2012). Similarly, to assess the UHI impact on energy usage, LST measurements must match with simulated data of hourly energy consumption from urban buildings (Zhou, Weng, Gurney, Shuai, & Hu, 2012). Thus, while

* Corresponding author at: Center for Urban and Environmental Change, Department of Earth and Environmental Systems, Indiana State University, Terre Haute, IN 47809, USA. Tel.: +1 812 237 2255; fax: +1 812 237 8029.
E-mail address: qweng@indstate.edu (Q. Weng).
[1] Tel.: +1 812 237 2255; fax: +1 812 237 8029.

http://dx.doi.org/10.1016/j.rse.2014.02.003
0034-4257/

some of the current satellite-borne TIR sensors can provide LST measurements at a reasonably high spatial resolution; their utilization in urban climate studies is restricted because of low temporal resolution and limited available nighttime image data (Stathopoulou & Cartalis, 2009). No single satellite system currently provides TIR data of global coverage that combines both high spatial and temporal resolutions. For a list of major current satellite TIR imaging systems, please refer to Tomlinson, Chapman, Thornes, and Baker (2011). Due to technical constraints, these sensing systems reflect a tradeoff between temporal and spatial resolution such that the systems with high-spatial resolution possess low-temporal resolution, or vice versa.

It is, therefore, highly desirable to develop techniques to derive LST data of high spatial and temporal resolutions from available remotely sensed data. Existing techniques have been named differently, including image merging, image/data fusion, spatial sharpening, downscaling, and disaggregation, but basically fall into two categories. While the spatial thermal sharpening techniques aim at downscaling (disaggregating) radiometric surface temperature of a sensor to higher resolutions typically associated with its shorter wavebands (visible and near-infrared) (Dominguez, Kleissl, Luvall, & Rickman, 2011; Kustas, Norman, Anderson, & French, 2003; Liu & Moore, 1998; Pu, Gong, Michishita, & Sasagawa, 2006), the temporal thermal sharpening techniques are developed to downscale TIR data from a coarser spatial-resolution but higher temporal-resolution sensor (typically associate with geostationary satellites) to generate highly temporally resolved LST diurnal cycles (Bechtel, Zakšek, & Hoshyaripour, 2012; Gottsche & Olesen, 2001; Inamdar & French, 2009; Inamdar, French, Hook, Vaughan, & Luckett, 2008; Zakšek & Oštir, 2012). The former can produce TIR data on the order of 10^1 to 10^2 m in spatial resolution but is limited by temporal resolution. The latter, on the other hand, can generate TIR data of up to every 15 min in temporal resolution, but usually have very coarse spatial resolution (e.g., 1000 × 1000 m). The inability of existing techniques in producing proper spatial and temporal sampling of LST data for urban climate and environmental studies calls for development of new techniques in TIR data fusion.

Downscaling is the scaling process of converting remote sensing data from a low to a high spatial resolution. Thermal downscaling is also named thermal *sharpening or disaggregating*. Thermal downscaling typically requires preserving the radiometry of original TIR radiance or LST data for subsequent data analysis (Stathopoulou & Cartalis, 2009). Therefore, it is important to understand the complexity and heterogeneity of thermal landscapes and key factors causing the spatial variability in LST. Optical and TIR data can provide complementary information about the Earth's surface, but due to instrumental reasons, TIR images are usually collected at coarser spatial resolution than do visible and near-infrared (NIR) bands on the same satellite platform. Various methods of thermal downscaling can be broadly grouped into physical and statistical approaches. Statistical downscaling techniques have been largely developed to disaggregate radiometric surface temperature of a sensor to higher resolutions associated with its shorter wavebands. Physical downscaling uses modulation methods, which take a thermal pixel as a block and distributes its thermal radiance into finer pixels corresponding to its shorter wavebands. Liu and Moore (1998) proposed the Pixel Block Intensity Modulation (PBIM) method, which were quantified by Landsat TM reflective bands, to adjust temperatures within the lower resolution pixel blocks of the TIR band based on topographic variations. Nichol (2009) suggested that the method by Liu and Moore is only suited for use within simple land-cover types where temperature variations are caused mainly by topography, but is not suitable for use in the urban areas where topography is mostly flat. Nichol (2009) proposed an alternative modulation method based on emissivity. Stathopoulou and Cartalis (2009) applied the PBIM method to downscale AVHRR LST image data to that of TM band 6 by employing different scaling factors (effective emissivity, season-coincident Landsat LST data, or their combination). It is found that the spatial pattern of the downscaled AVHRR LST resembled reasonably well with time-coincident TM LST and the root mean square error (RMSE) yielded a range of 4.9 to 5.3 °C. It is worthy to note that Liu and Pu (2008) compared the modulation method with spectral unmixing of TIR radiance. The former disaggregated TIR radiance by using higher spatial resolution land cover data as the distribution factor, while the latter employed spectral mixture analysis (SMA) to decompose mixed TIR pixels into multiple isothermal components. However, the spatial details within mixed pixels remained unresolved in the decomposed component temperatures (Gillespie, 1992). Moreover, the isothermal assumption that underpins various modulation methods for retrieving component temperature or emissivity may not be valid. This is especially true within urban landscapes where component surfaces are often seen smaller than the IFOV of satellite sensors, resulting in a mixture of different temperature components.

While these thermal downscaling methods provide useful means to improve the resolution of TIR data of a sensor or LST to higher spatial resolutions, they do not enhance the temporal resolution of the sensor simultaneously. Gao, Masek, Schwaller, and Hall (2006) developed a data fusion technique that allows improving spatial resolution and temporal coverage at the same time. The technique was named "Spatial and Temporal Adaptive Reflectance Fusion Model", or for short, STARFM, that blends Landsat and MODIS data to generate synthetic Landsat-like daily surface reflectance. The basic assumption is that surface reflectance at a predicted date may be estimated by a weighted sum of the spectrally similar neighborhood information from both Landsat and MODIS reflectance at observed dates (close to the predicted date). Essentially, STARFM integrates daily information from MODIS with periodic Landsat data to interpolate surface reflectance at the Landsat resolution of 30 m on a daily basis. This data fusion approach has received a lot of attention lately, because it can provide successful monitoring of seasonal changes in vegetation cover (Gao et al., 2006; Hilker et al., 2009) and larger changes in land use (Hansen et al., 2008; Potapov, Hansen, Stehman, Loveland, & Pittman, 2008). The STARFM approach was later adjusted and revised for specific applications under different conditions. Hilker et al. (2009) developed Spatial Temporal Adaptive Algorithm for mapping Reflectance Change (STAARCH) model based on the STARFM approach for mapping disturbance events between two input dates. The forest changes are mapped using the dense time-series of MODIS imagery. Moreover, the STAARCH allows selecting an optimal MODIS–Landsat image pair from one of two inputs for making a prediction (Hilker, Wulder, Coops, Linke, et al., 2009). Zhu, Chen, Gao, Chen, and Masek (2010) developed an enhanced STARFM (ESTARFM) approach for application in a heterogeneous area by introducing a conversion coefficient to the fusion model, which represented the ratio of change between the MODIS pixels and ETM+ end-members. The ESTARFM approach provides a solution for the heterogeneous (mixed) pixels, but it still cannot accurately predict short-term, transient changes not recorded in any of the bracketing (observed) fine-resolution images (Zhu et al., 2010).

Although STARFM was originally designed to fuse shortwave reflectance fields from MODIS and Landsat to create daily reflectance and vegetation index maps, it appears to hold great utility for high-resolution thermal mapping too (Anderson et al., 2011; Liu & Weng, 2012). Anderson et al. (2010) used STARFM to predict evapotranspiration at 30-m resolution and compared it with flux estimation derived from spatially disaggregated ALEXI (Atmosphere–Land Exchange Inverse) model. They found that the prediction yielded errors on the order of 10%. Liu and Weng (2012) applied the STARFM model to simulate ASTER-like land surface reflectance and LST images for Los Angeles for five dates in the five epidemiological weeks in summer 2007, and used the simulated data to assess the environmental conditions of the WNV (West Nile Virus) outbreak. The mean absolute difference between the observed and the simulated surface reflectance was found less than 0.2 and the LST residual less than 1 °C for all images. However, the application of the STARFM and its variants for LST prediction is immature in terms of methodology. Many critical issues have not been

solved, especially in terms of thermal landscape heterogeneity, land cover change, and vegetation phenology. Moreover, LST of a landscape patch may be affected by the surrounding materials seriously (Oke, 1982). In this research, we intend to develop a new fusion algorithm for TIR data to predict daily LST at 120-m resolution by blending Landsat TM and MODIS LST data, i.e., SADFAT. Following a brief introduction of the study area, Sections 3 and 4 will discuss about the theoretical basis of the proposed data fusion model and the implementation issues of the algorithm. The results will be presented in Section 5, followed by Discussion and conclusions.

2. Study area and data

The study area covers the majority of the Los Angeles County, California, USA, a small portion of Simi Valley in Ventura County and a small part of Orange County (Fig. 1). This area consists of various land covers, including water, developed urban, barren land, forest, shrub land, herbaceous, planted/cultivated, and wetlands as identified by the 2006 NLCD database. The primary mountain ranges are Santa Monica Mountains and the San Gabriel Mountains in the southwestern and southeastern part of Los Angeles County, respectively. The valleys are largely the population centers, and compose a large percentage of the urban areas. The area possesses a Subtropical–Mediterranean climate with a dry summers and moist winters. The average high air temperature is 29 °C in August and 20 °C in January based on the weather records from the Downtown-University of Southern California campus. According to a study by the urban heat island group, the urbanization of city has negatively affected the urban community, such as the increased energy use, impaired air quality, and the aggravation of heat-related and respiratory illness (http://heatisland.lbl.gov/coolscience/cool-science-urban-heat-island). Thus, the generation of daily LST data will be conducive to monitoring the dynamic patterns of LST and to investigating the UHI effect on energy use and environmental and public health.

Landsat TM images of Path 41, Row 36 acquired on 24th June, 10th July, 27th August, 28th September, 14th October, 30th October, and 15th November, 2005 were used as reference data to estimate daily LST images at 120 m resolution (Table 1). The corresponding daily MODIS LST (MOD11A1) and reflectance data (MOD09GA) were obtained through the Level 1 and Atmosphere Archive and Distribution System website data portal available at http://ladsweb.nascom.nasa.gov/data/search.html. These MODIS LST products were selected and used as another set of references for the daily LST mapping. Before the implementation of the fusion method, both the Landsat TM and MODIS data were registered to the same coordinate system and resampled to the same spatial resolution (120 m). A shared cloud mask was created for both Landsat and MODIS images to remove cloudy pixels from the computation.

3. Methodology

3.1. Theoretical basis of the TIR data fusion model

The STARFM algorithm was initially designed to predict surface reflectance and is based on the assumption that MODIS and Landsat surface reflectance are highly consistent (Gao et al., 2006; Masek et al., 2006). For homogeneous pixels, as long as this assumption holds true for the thermal regime, the STARFM procedure can be applied to TIR image data either at radiance or at LST level. Since our improved method must handle the heterogeneous characteristics of LSTs and radiance can

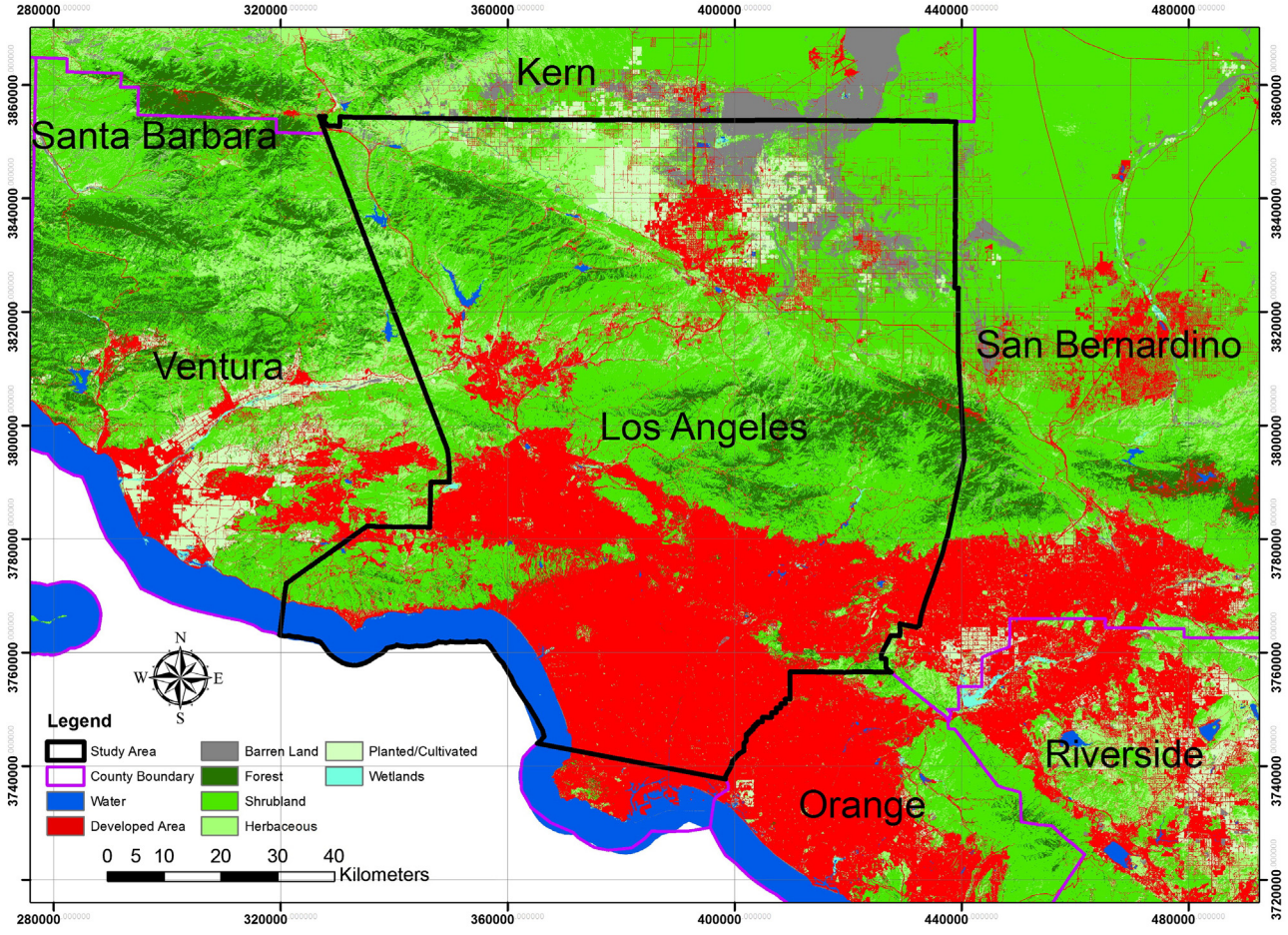

Fig. 1. The study area Los Angeles County, California, USA. The background image shows land cover types derived from the NLCD 2006.

Table 1
Characteristics of Landsat and MODIS LST data used in the study.

Date	Landsat overpass time (H:M)	MODIS overpass time (H:M)	Landsat Min	Landsat Median	Landsat Max	MODIS Min	MODIS Median	MODIS Max	Correlation
06/24/2005	10:15	10:06	259.51	313.60	333.75	250.72	310.54	319.24	0.83
07/10/2005	10:16	10:06	283.38	309.27	331.37	250.00	306.46	317.80	0.67
08/27/2005	10:16	10:06	278.19	318.53	341.76	250.02	315.04	322.02	0.77
09/28/2005	10:16	10:06	263.60	310.56	329.32	252.66	307.48	314.44	0.79
10/14/2005	10:16	10:06	268.78	310.79	334.94	254.20	308.46	319.38	0.63
10/30/2005	10:16	10:06	257.50	299.33	320.01	250.02	297.62	306.48	0.66
11/15/2005	10:16	10:06	261.07	299.12	319.16	250.16	298.00	304.82	0.75

Note: The over-passing time recorded is the local time in the format of hour and minute, and the unit for the minimum, median, and maximum LST values is Kelvin (K).

be spatially aggregated using linear form, this research focuses on data fusion at the radiance level. For homogenous pixels, remotely sensed TIR data from different sensors at a close acquisition time should be comparable and correlated after radiometric calibration, geometric rectification, and atmospheric correction. Nevertheless, such factors as acquisition time, bandwidth, orbit parameters, geo-location errors, effective pixel coverage, and spectral response function can introduce some system biases into the subsequent analysis. Assuming that MODIS radiance images have been resampled to the same spatial resolution of Landsat radiance images, the following discussion focuses on how to derive daily radiance images at 120-m resolution. For the convenience, the MODIS pixel will be described as *M* pixel, and the Landsat pixel will be simply described as *L* pixel.

For a homogeneous *M* pixel covered only by one land cover type, the radiance difference between the resampled *M* pixel and the *L* pixel results from the system biases and should be stable in a short period. Thus, the relationship between the observations of radiance from the two sensors for the homogeneous pixels can be expressed as:

$$R_L(x,y,t) = a * R_M(x,y,t) + b \tag{1}$$

where *R* defines the radiance, (x, y) represents a given location, *t* is the *acquisition* date, and *a*, *b* are the coefficients for relative adjustment needed for the Landsat and MODIS radiance pixels. Therefore, suppose there is one pair of Landsat and MODIS image acquired at t_0, and another MODIS image acquired at t_p, and the land cover and sensor calibration does not change during the period between t_0 and t_p, then Eq. (1) can have two instances:

$$R_L(x,y,t_0) = a * R_M(x,y,t_0) + b \tag{2}$$

$$R_L\left(x,y,t_p\right) = a * R_M\left(x,y,t_p\right) + b. \tag{3}$$

There is a possibility that the relationship between MODIS and Landsat LST may vary from day to day depends on weather and surface moisture conditions. Table 1 shows that the relationship remained stable as indicated by correlation coefficient (Masek et al., 2006). Thus, the inference of Eqs. (2) and (3) is reasonable.

From Eqs. (2) and (3), the following expression can be derived:

$$R_L\left(x,y,t_p\right) = R_L(x,y,t_0) + a * \left[R_M\left(x,y,t_p\right) - R_M(x,y,t_0)\right]. \tag{4}$$

Eq. (4) states that for a homogenous pixel at t_p, its *L* radiance equals to the sum of *L* radiance at t_0 and the scaled difference of *M* radiance between t_0 and t_p. The coefficient *a* can be calculated from the system biases given the stability of the two sensors. If two pairs of *L* image and *M* image can be obtained, the coefficients can also be determined by the regression of the *L* radiance with *M* radiance at t_1 and t_2. However, it should be noted that Eq. (4) is only valid for the non-changing surfaces if the relationship between MODIS and Landsat LST remains stable.

However, a large proportion of the pixels from medium- and coarse-resolution imagery contain more than one land cover type, i.e., they are mixed pixels. According to linear spectral mixture analysis (LSMA) theory, the radiance of a mixed pixel can be defined as:

$$R = \sum_{i=1}^{N} f_i R_i + \varepsilon \tag{5}$$

where *R* represents the radiance received by the satellite sensor, *N* is the number of end-member, f_i denotes the fraction of each land cover component, and ε is the residual. Suppose that each *L* pixel can be regarded as one end-member of a *M* pixel, then the radiance of the *M* pixel at t_1 and t_2 can be described as Eqs. (6) and (7), according to Eqs. (1) and (5):

$$R_M(t_1) = \sum_{i=1}^{N} f_i \left(\frac{1}{a} R_L(t_1) - \frac{b}{a}\right) \tag{6}$$

$$R_M(t_2) = \sum_{i=1}^{N} f_i \left(\frac{1}{a} R_L(t_2) - \frac{b}{a}\right). \tag{7}$$

It should be noted that in Eqs. (6) and (7), the coefficients *a* and *b* remain stable and the fraction of each *L* pixel end-member does not vary, either. Therefore, the radiance change of an *M* pixel from t_1 to t_2 can be computed as:

$$R_M(t_2) - R_M(t_1) = \frac{1}{a} \sum_{i=1}^{N} f_i (R_{iL}(t_2) - R_{iL}(t_1)). \tag{8}$$

The temporal variability of LST shows a strong diurnality (Sabins, 1997) and seasonality (Weng, Liu, Liang, & Lu, 2008). The LST seasonal change can be modeled using the annual temperature cycle (ATC) approximated by a sinusoidal function (Bechtel, 2012):

$$\mathrm{LST} = MAST + YAST * \sin(w * d + \theta) \tag{9}$$

where *MAST* is the mean annual surface temperature, *YAST* is the yearly amplitude surface temperature, *w* is the angular frequency, *d* is the day of year (DOY) relative to the equinox and θ is the phase shift. Since spectral radiance is related to LST by the Plank's law, the radiance change of an *L* pixel from time t_1 to t_2 can be quantified as:

$$R_{iL}(t_2) - R_{iL}(t_1) = 2c \cos\left(\theta_i + w\frac{d_1 + d_2}{2}\right) \sin w\frac{d_2 - d_1}{2} = C \cos\left(\theta_i + w\bar{d}\right) \tag{10}$$

where θ is the phase shift, or heat lag, *c* is the amplitude of the radiance variation, *C* is the constant, and $\bar{d}$ is the mean acquisition date, d_1 and d_2

are the parameters input to the algorithm. Incorporating the ATC model, Eq. (8) can be re-written as:

$$R_M(t_2)-R_M(t_1)=\frac{2c\sin w\left(\frac{d_2-d_1}{2}\right)}{a}\sum_{i=1}^{N}f_i\cos\left(\theta_i+w\bar{d}\right)=\frac{C}{a}\sum_{i=1}^{N}f_i\cos\left(\theta_i+w\bar{d}\right). \quad (11)$$

If the radiances of the kth L pixel at date t_1 and t_2 are known, Eq. (9) has an instance as:

$$R_{kL}(t_2)-R_{kL}(t_1)=2c\cos\left(\theta_k+w\bar{d}\right)\sin w\frac{d_2-d_1}{2}. \quad (12)$$

By combining Eq. (11) with Eq. (12), Eq. (13) can be obtained:

$$\frac{R_{kL}(t_2)-R_{kL}(t_1)}{R_M(t_2)-R_M(t_1)}=\frac{\cos\left(\theta_k+w\bar{d}\right)}{\frac{1}{a}\sum_{i=1}^{N}f_i\cos\left(\theta_i+w\bar{d}\right)}=h_k. \quad (13)$$

Since θ reflects the phase shift of a pixel and is associated with the thermal properties of land surface materials, it can be regarded as constant as long as the land cover does not change in the observational period. Therefore, the ratio of the radiance change of kth L pixel to that of the corresponding M pixel is constant for a certain L pixel. Here, h_k is called the conversion coefficient for the purpose of consistency (Zhu et al., 2010).

Based on Eq. (13), if one pair of L and M radiance image at t_0 and another M radiance image at t_p are available, the L radiance image at t_p can be predicted using the following formula:

$$R_L\left(x,y,t_p\right)=R_L(x,y,t_0)+h(x,y)*\left[R_M\left(x,y,t_p\right)-R_M(x,y,t_0)\right]. \quad (14)$$

Apparently, Eqs. (4) and (13) only utilize information from a single pixel to infer the L radiance. By introducing additional information from neighboring spectrally similar pixels, the solution to Eq. (14) can be determined uniquely, and a moving window (Gao et al., 2006) can be employed to compute the radiance of the central pixel. Therefore, assuming w is the moving window size, the predicted L pixel radiance can be computed as:

$$R_L\left(x_{w/2},y_{w/2},t_p\right)=R_L\left(x_{w/2},y_{w/2},t_0\right)+\sum_{i-1}^{N}W_i*h_i*\left[R_M\left(x_i,y_i,t_p\right)-R_M(x_i,y_i,t_0)\right] \quad (15)$$

where W_i is the weight of a neighboring similar pixel, and N is the number of the spectrally similar pixel. The computed radiance can then be converted to LST using the Planck's law. It deserves to note that the use of ATC parameters ignores the influence of synoptic and surface conditions on the variations of the thermal radiance; however, since Eq. (10) has coped with the change of radiance, it is reasonable to assume the stability of the synoptic and surface conditions.

Fig. 2 illustrates the procedure of SADFAT, which contains five steps. The inputs for the algorithm are two pairs of L and M images at t_1 and t_2, respectively and one M image at the prediction date t_p. At the first step, all the images should be registered to the same coordinate system and atmospherically calibrated and corrected to the surface radiance. Secondly, the two L images are used to search for the spectrally similar pixels according to the predefined principles. The third step is to compute the combined weight for each similar pixel. At the fourth step, the conversion coefficients are determined by the regression analysis. Finally, the M images at t_p and the calculated conversion coefficients are employed to obtain the predicted L radiance image. The computed radiance image will then be converted to LST using the Planck's law. The predicted LST images are validated against the real TM image data using the coefficient of correlation, mean difference, and mean absolute difference values.

3.2. LST retrieval for Landsat TM imagery

The accuracy of LST computation for Landsat TM image is crucial in implementing the proposed algorithm. Sobrino, Jimenez-Munoz, and Paolini (2004) investigated and compared three methods to derive LST over an agricultural area in Spain with land surface emissivity estimated from the visible and near infrared bands. The retrieved results disclosed that the error of the single channel method developed by Jimenez-Munoz and Sobrino (2003) in retrieving LST is below 1 K. Therefore, the generalized single channel method was utilized for LST estimation in this study.

The main characteristic of the generalized single channel method is that in situ radio-soundings or effective mean atmospheric temperature values are not required compared to other single channel methods. More importantly, specific atmospheric functions for Landsat TM 6 were obtained using the TIGR database and simulations from MODTRAN 3.5. The following equations show how to implement the single channel method for TM TIR data.

$$T_s=\gamma\left[\varepsilon^{-1}(\psi_1L_{sensor}+\psi_2)+\psi_3\right]+\delta \quad (16)$$

with

$$\gamma=\left(\frac{c_2}{T_{sensor}^2}\left[\frac{\lambda^4}{c_1}L_{sensor}+\lambda^{-1}\right]\right)^{-1} \quad (17a)$$

$$\delta=-\gamma L_{sensor}+T_{sensor} \quad (17b)$$

where L_{sensor} is the at-satellite radiance, T_{sensor} is the at sensor brightness temperature, λ is the effective wavelength for TM sensor (11.475 μm), c_1, c_2 are the constants. The atmospheric functions are defined based on the water vapor content:

$$\begin{bmatrix}\psi_1\\ \psi_2\\ \psi_3\end{bmatrix}=\begin{bmatrix}0.14714 & -0.15583 & 1.1234\\ -1.1836 & -0.37607 & -0.52894\\ -0.04554 & 1.8719 & -0.39071\end{bmatrix}\begin{bmatrix}\omega^2\\ \omega\\ 1\end{bmatrix} \quad (18)$$

where ω is the water vapor content, which can be obtained from the satellite images or in situ device (Jimenez-Munoz & Sobrino, 2003). Since MODIS can provide data of water vapor content, this research adopted the ratio method using the atmospheric water channels (Kaufman & Gao, 1992) to provide the input for the atmospheric function.

Another parameter assumed to be known in the single channel method is land surface emissivity (LSE). According to Sobrino and Raissouni (2000), it is possible to acquire LSE data from NDVI values for the areas comprised of soil, vegetation and mixed soil/vegetation components. The problem of the NDVI threshold method, as pointed out by Sobrino et al. (2008), is the lack of continuity emissivity values at soil and vegetation thresholds. Therefore, a simplified version of the NDVI threshold method was employed in this study for the derivation of LSE data. The values of NDVI for soil and vegetation were obtained from the NDVI histogram of each image. However, the NDVI threshold method is not suitable to derive emissivity values for the urban areas. Therefore, the emissivity data product from the ASTER Global Emissivity Database 3.0 (Hulley & Hook, 2009; Hulley, Hook, & Baldridge, 2008) was utilized for the urban areas identified by the National Land Cover Database 2006. The mean emissivity value of Bands 13 and 14 was selected for use to match the spectral range of TM Band 6. The original emissivity product was delivered in 1° by 1° tiles with geographic projection (WGS84) at 100 m spatial resolution. It was later mosaicked and resampled to 120 m using UTM projection system to match the

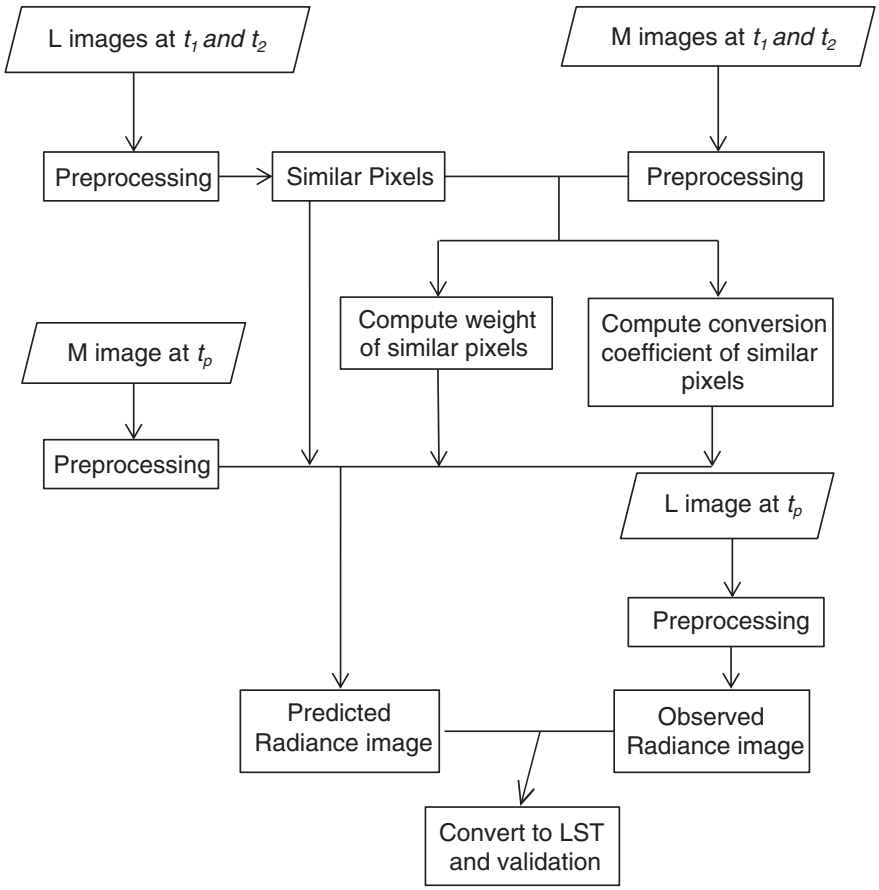

Fig. 2. The SADFAT procedure for predicting the daily LST image and the validation. Landsat images at t_1 and t_2 are first pre-processed and used for selection of similar pixels. The selected similar pixels are then combined with MODIS images at t_1 and t_2 to compute weight and conversion coefficient. The prediction can be made based on the MODIS images at a prediction date (t_p).

Landsat LST data. It should also be noted that the study area contains open water and inland lakes, which are not suitable for the direct use of the threshold method either. As a result, water areas were first extracted based on their spectral characteristics because water bodies have a low value for the infrared reflectance and NDVI (Jensen, 2005). The effective emissivity value was calculated for water bodies by using the ASTER spectral library 2.0 and the TM spectral response filter. The Kirchhoff's law was applied to convert hemispherical reflectance to surface emissivity (Nicodemus, 1965).

4. Model implementation

The implementation of SADFAT requires pre-processing of Landsat and MODIS data, selection of spectrally similar pixels, and computation of the conversion coefficient. The calculation of weights for spectrally similar pixels involves weighing the contribution of the neighboring pixels to the computation of a central pixel. The conversion coefficient reflects the combined changes of LST for Landsat and MODIS from one date to another. Using a local moving window, neighboring spectrally similar pixels were included for the computation of the LST for a central pixel with the temporal weights of the two dates. Below are the detailed descriptions for the implementation of SADFAT.

4.1. Data preprocessing and selection of spectrally similar pixels

Before the application of SADFAT, both MODIS and Landsat data need to be pre-processed geometrically to the same pixel size and radiometrically to ensure the data accuracy. In this study, Landsat level 1 T product was employed and atmospherically calibrated (Bands 1–5 and 7) using Landsat Ecosystem Disturbance Adaptive Processing System (LEDAPS) (Masek et al., 2006). The LST retrieval for Landsat TM was based on the single channel method described in Section 3.2. MODIS daily LST and surface reflectance data were re-projected to the Landsat coordinate system using the MODIS Reprojection Tools (MRT).

Similar pixels provide needed spectral and spatial information for the LST computation of a central pixel within the local moving window. In the original STARFM and the enhanced STARFM models (Gao et al., 2006; Zhu et al., 2010), two methods were used to obtain spectrally similar pixels. The unsupervised classification can be applied to Landsat images to identify the pixels belonging to the same cluster as the central pixel. Another method is to define a threshold of difference between the central pixel and the neighboring pixels, through which similar pixels can be identified. Differences among the spectrally similar pixels were computed based on the standard deviation of fine resolution images and the number of classes used (Gao et al., 2006). A larger number of classes mean a stricter condition for selecting spectrally similar pixels. Since this study utilized multiple bands, i.e., Landsat red, NIR, and TIR bands, to search for similar pixels, it is reasonable to adopt the threshold method. The threshold method can avoid global misclassifications which would have an adverse impact on the calculation (Gao et al., 2006). In searching for the similar pixels, both Landsat images were used to provide the effective similar pixels. If only one Landsat image was used for the identification of similar pixels, it may result in inconsistency with the actual surface conditions, e.g., land cover may change from one date to another date. In addition, it is possible that a certain pixel did not have any spectrally similar pixel. In such case, the weight for the central pixel would be set to 1. It is also possible that all of the similar pixels cannot provide better prediction than the central pixel.

Therefore, additional filtering was applied to the selected candidates to remove the poor quality pixels (Gao et al., 2006). First, according to the QA layer in Landsat and MODIS data (surface reflectance and LST product), poor quality data were removed. Second, neighboring similar pixels were filtered out if they cannot provide better reflective and thermal information than the central pixel.

4.2. Computation of weight

The weight defined the contribution of neighboring pixels to the calculation of a central pixel. It was determined by the location of the similar pixels and the reflective and thermal similarity between the fine and coarse resolution data. Higher reflective and thermal similarity and shorter distance between a central and a neighboring pixel yielded a higher weight in the computation. This research computed the correlation coefficient to determine the reflective and thermal similarity between Landsat and the corresponding MODIS pixels. The correlation coefficient can be computed as:

$$R_i = \frac{E[(L_i - E(L_i))(M_i - E(M_i))]}{\sqrt{D(L_i)}\sqrt{D(M_i)}} \tag{19a}$$

with

$$L_i = [L_i(x,y,t_1,B_1),\ldots,L_i(x,y,t_1,B_n),\ \ L_i(x,y,t_2,B_1),\ldots,L_i(x,y,t_2,B_n)] \tag{19b}$$

$$M_i = [M_i(x,y,t_1,B_1),\ldots,M_i(x,y,t_1,B_n),M_i(x,y,t_2,B_1),\ldots,M_i(x,y,t_2,B_n)] \tag{19c}$$

where R_i is the combined reflective and thermal correlation coefficient between L and M images for the ith pixel. L_i and M_i are the collection of similar pixels from Band 3, Band 4 and Band 6 for Landsat and its corresponding bands for MODIS at t_1 and t_2. E and D are the value of expectation and variance, respectively. The value of R ranged from −1 to 1, and a higher R meant a higher reflective and thermal similarity. The reasons to include both the reflective and thermal bands of different dates were: (1) LST varied with land cover type (Weng, Lu, & Schubring, 2004). The inclusion of additional spectral bands ensured that the selection and computation only occurred for the same land cover. (2) Both pairs of L and M images were contained in the vectors to provide a more accurate calculation of similarity given that land cover may change over the time.

The location of similar pixels also impacted their contributions to a central pixel. The distance between the central pixel and the neighboring ith pixel can be calculated as:

$$d_i = 1 + \sqrt{\left(x_{w/2} - x_i\right)^2 + \left(y_{w/2} - y_i\right)^2}/(w/2) \tag{20}$$

where d_i is the computed distance and ranges from 1 to $2^{0.5}$, $(x_{w/2}, y_{w/2})$ is the spatial position of the central pixel (x_i, y_i), is the position of the ith neighboring similar pixel. With the location of the similar pixels and the reflective and thermal similarity, a combined weight, CW, can be calculated as:

$$CW = (1 - R_i) * d_i. \tag{21}$$

A spectrally similar pixel with a larger CW value would have a less weight in the calculation. Therefore, the combined weight needs to be normalized based on the inverse:

$$W_i = (1/CW_i)/\sum_{i=1}^{N} 1/CW_i \tag{22}$$

W_i is the final combined weight for the ith similar pixel. The range of W ranged from 0 to 1, and the total value of each W_i would be 1. When there were p similar pixels among all the similar pixels whose corresponding coarse resolution pixels were pure ($R = 1$), the weight for the similar p pixels would be set to $1 / p$ and other pixels to 0. That is to say, only homogeneous pixels were used for the calculation of the weight.

4.3. Conversion coefficient and computation of LST for the central pixel

The conversion coefficient defines the relationship between L and M radiance changes (Zhu et al., 2010). Since neighboring similar pixels are introduced, it is practical to compute the conversion coefficient using the regression analysis within each local moving window. Regression analysis is reasonable, because, based on the theoretical basis of SADFAT, similar pixels within the same coarse resolution pixel have the same conversion coefficient. Due to the additional spatial filter, it is suitable to calculate the conversion coefficients using all the selected similar pixels rather than using only similar pixels within the same coarse resolution. Considering the potential geometrical error involved in the data pre-processing, we decided to compute the conversion coefficient for all the selected similar pixels. As a special case, if there were no similar pixels or a linear regression model cannot be built with the defined statistical significance, the central pixel can still provide the conversion coefficient although this may introduce some errors.

According to Eq. (15), L radiance image at t_p can be predicted based on the weighted scaled M radiance changes and L radiance image either at t_1 or t_2. An accurate radiance image can be obtained by using the weighted combination of the two predicted radiance images based on t_1 and t_2, while the temporal weights of the two images may be given by the temporal changes in coarse resolution radiance images. Eq. (23) shows how to calculate the temporal weight:

$$T_k = 1/\left(\frac{\sum_{i=1}^{w}\sum_{j=1}^{w} M\left(x_i,y_j,t_k,B\right) - \sum_{i=1}^{w}\sum_{j=1}^{w} M\left(x_i,y_j,t_p,B\right)\Big)}{\sum_{k=t_i,t_2} 1/\left(\sum_{i=1}^{w}\sum_{j=1}^{w} M\left(x_i,y_j,t_k,B\right) - \sum_{i=1}^{w}\sum_{j=1}^{w} M\left(x_i,y_j,t_p,B\right)\right)}\right) \tag{23}$$

where $M(x, y, t, B)$ is the resampled radiance at time t. Therefore, the final predicted radiance image can be calculated as follows:

$$L\left(x_{w/2}, y_{w/2}, t_p\right) = T_{t_1} * L_{t_1}\left(x_{\frac{w}{2}}, y_{\frac{w}{2}}, t_p\right) + T_{t_2} * L_{t_2}\left(x_{\frac{w}{2}}, y_{\frac{w}{2}}, t_p\right) \tag{24}$$

where L_{t_1} is the predicted radiance image using L image at t_1 as the base image, L_{t_2} is the predicted radiance image using L image at t_2 as the base image. With the final radiance image, LST image can be computed.

5. Results

The accuracy of SADFAT was evaluated through validating the predicted LSTs against the observed LSTs obtained from the Landsat TIR data. In this study, five pairs of Landsat and MODIS images were used for accuracy assessment. We selected correlation coefficient, mean difference and mean absolute difference to serve as indicators to evaluate the accuracy. Two pairs of MODIS and Landsat images, acquired on 24th June and 15th November, 2005, respectively, were used as the first inputs to the fusion model (Fig. 3). The white areas in the LST images were masked-out cloudy areas according to the QA layer of the MODIS data. From Fig. 3, it is apparent that LST spatial patterns in MODIS and Landsat images were substantially different in the two dates. Although the minimum temperatures of MODIS and Landsat images seemed similar, the maximum temperatures differed in about 15° in either date (Table 1). Considering the land cover characteristics of the study area, the size of the searching window was set to 3 MODIS pixels (i.e., 25 Landsat TM pixels) and the number of land cover types was set to 5. The second input for the fusion model was the MODIS LST image used

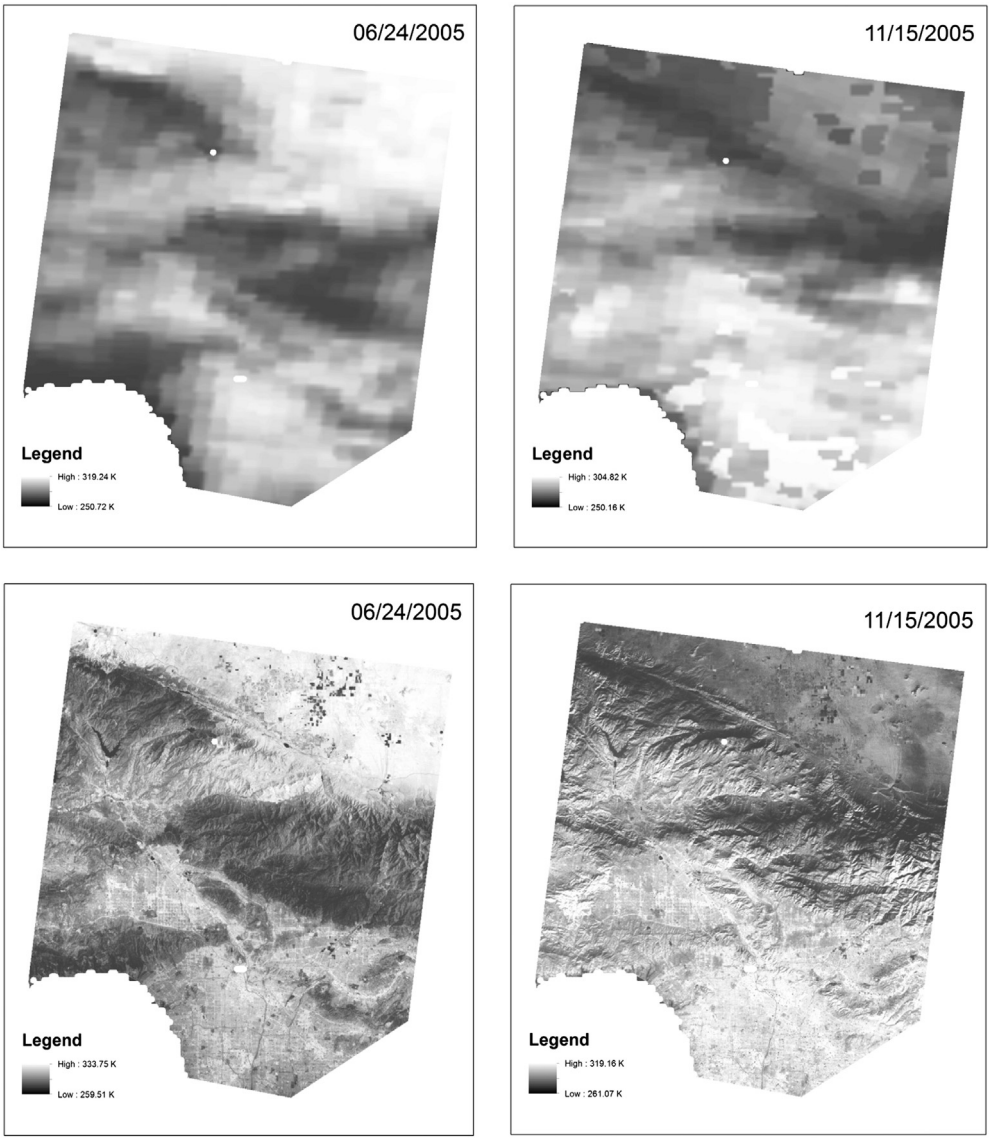

Fig. 3. The observed MODIS (upper row) and Landsat (lower row) LST images on 06/24/2005 and 11/15/2005 as the base images for the fusion model. White points were identified and masked out according to the QA layer of MODIS LST product.

to predict the corresponding Landsat LST image at the same date (t_p). Fig. 4 showed the results of prediction in comparison with the inputs: (A) MODIS LST images (model inputs); (B) predicted Landsat LST images; and (C) observed Landsat LST images on 10th July, 27th August, 28th September, 14th October, and 30th October, 2005, respectively. For all the five predictions, the predicted LST images (B) and the observed LST images (C) matched well in terms of the overall spatial patterns of LST. The predicted LST images contained the vast majority of the spatial details found in the observed images, including such surface features as roads, urban streets, and lakes. Moreover, LST variations with terrain were also preserved and the unique LST patterns in the mountainous region can also be discerned.

Fig. 5 displays the scatter plots between the predicted and observed LSTs for each prediction date. The data points fell close to the diagonal line in each panel, indicating that the predictions were all in good agreement with the observations. To quantify the prediction accuracy, correlation coefficient, mean difference, and mean absolute difference were computed. Table 2 shows the result of computation. Overall, the values of mean difference and mean absolute difference between the predicted and the observed LSTs were quiet small; whereas the correlation coefficient values were all found to be greater than 0.90, except for the one on 14th October, 2005. This is because that the correlation between MODIS and Landsat LST on that date was the weakest (0.63), as seen in Table 1. Because all the predictions shared the same pairs of Landsat and MODIS LST images as the model inputs, a comparison of their accuracies was also feasible. The mean absolute difference ranged from 1.25 K to approximately 2.0 K. Since the selected images reflected well the phenological change from June to November, SADFAT proved to be effective to account for the temporal variations of LST. Compared with previous studies using the original STARFM method (Liu & Weng, 2012) or with a revised filter considering surrounding pixels to predict LST (Huang, Wang, Song, Fu, & Wong, 2012), the improvement of LST prediction in this study was due largely to the inclusion of the ATC model and LSMA into the fusion algorithm to calculate the conversion coefficient. The ATC model can delineate the trend of annual mean temperature variations while ignoring the specific daily LST changes (Bechtel, 2012; Weng & Fu, 2014), and thus facilitated the prediction of LST temporal changes between the two dates. However, it should be noted in the scatter plots that there were some pixels showing large differences between the predicted and observed LSTs. These discrepancies presented a major limitation of SATFAT that associated with the assumption on the stability of phase shift parameter (θ) in the ATC model. While it may be largely true that the land cover and other surface conditions did not change over the study period; however, if land covers or other surface

conditions did change, it could lead to some errors in the prediction. We identified some of the pixels with large values in mean difference and mean absolute difference, and found that all those pixels had undergone land cover changes during the study period. Fig. 6 illustrated that vegetated areas on 06/24/2005 changed to bare soil on 11/15/2005. Since land cover altered over the two imaged dates and the ATC model was not able to capture the change in LST, a large prediction error occurred.

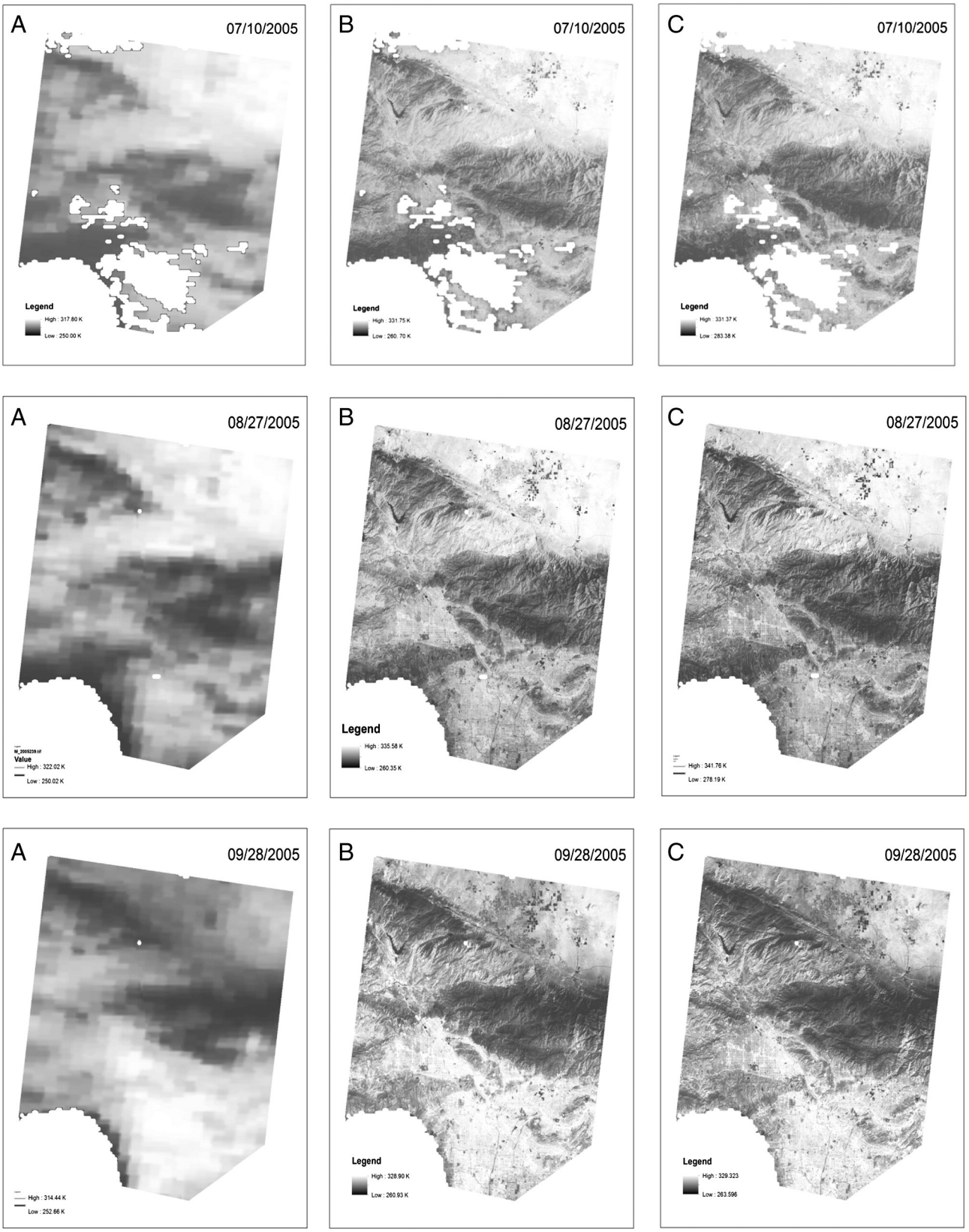

Fig. 4. (A) The observed MODIS LST images; (B) the predicted Landsat LST images; and (C) the observed Landsat LST images on 07/10/2005, 08/27/2005, 09/28/2005, 10/14/2005, and 10/30/2005, respectively. White areas were identified and masked out according to the QA layer of the MODIS data product.

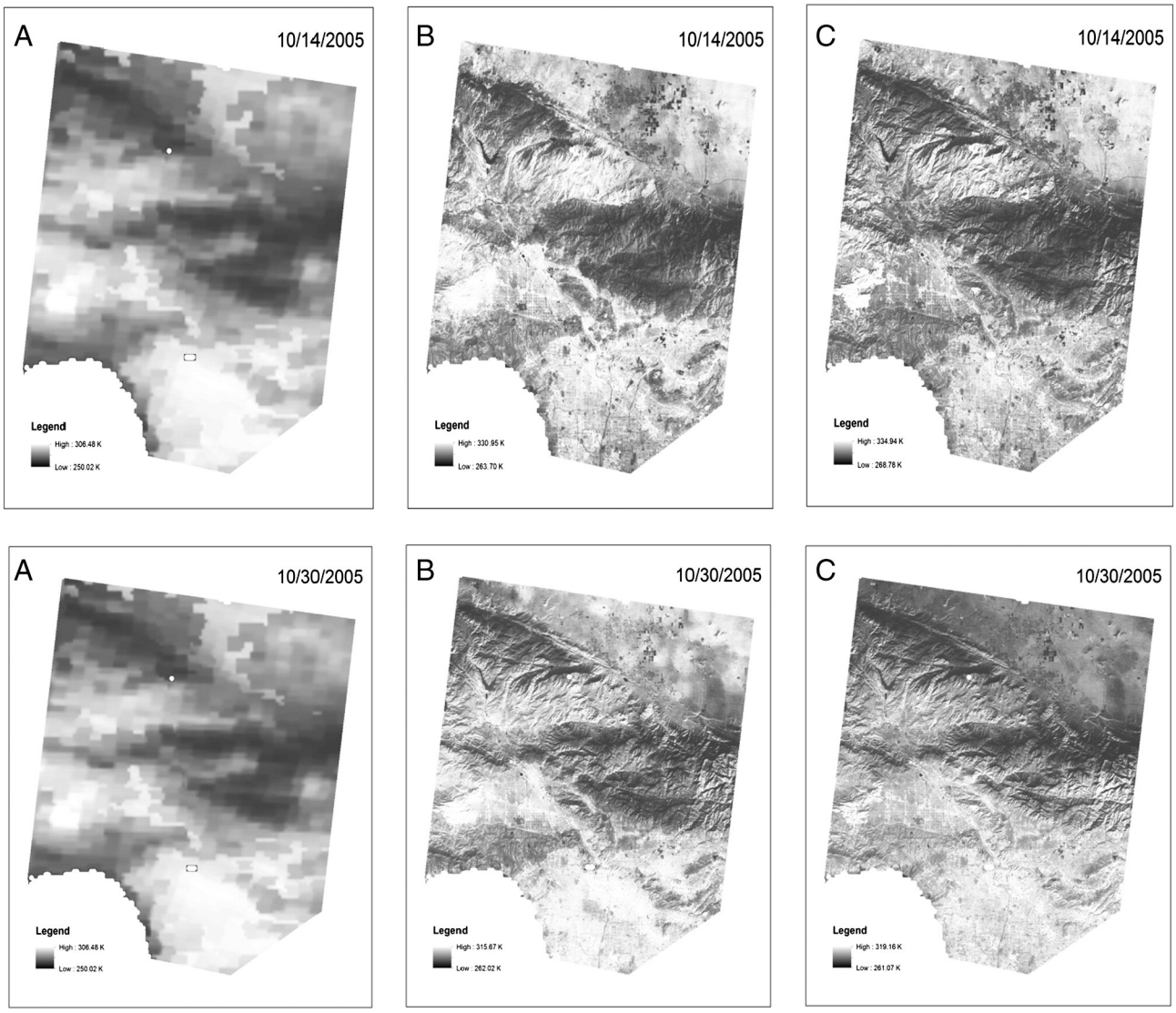

Fig. 4 (*continued*).

6. Discussion and conclusions

This research proposed a data fusion model, SADFAT, for predicting LSTs at high temporal frequency and at the medium spatial resolution (120 m) using the combined datasets of MODIS and Landsat. The STARFM algorithm, which was devised for producing Landsat time series surface-reflectance product, was modified and improved for generating LST data product, with special attention paid to the annual cycle of LST and the landscape heterogeneity in the urban areas. This paper has examined in details the theoretical basis and the implementation procedures of SADFAT, and performed an experiment that predicted LSTs of five dates in 2005 from July to October in the Los Angeles County, California. The result, as measured by the mean absolute difference, suggests that the prediction accuracy yielded from 1.25 K to 2 K.

SADFAT presented several improvements over its precedents. The most significant improvement was to incorporate an ATC model to characterize the annual variations of LST, based on which the conversion coefficients were computed. The use of a conversion coefficient allowed relating the thermal radiance change of a mixed pixel at the coarse resolution to that of a fine resolution pixel. In this way, the prediction with a regression model can well be justified. In contrast with the ESTARFM (Zhu et al., 2010) that used a linear model to predict the change in surface reflectance, SADFAT employed a non-linear model to approximate annual change of LST. In addition, since SADFAT aims at prediction of LSTs, both the reflective (Landsat bands 3 and 4) and TIR bands were utilized for searching for similar pixels. The inclusion of the TIR band allowed for the obtainment of more accurate similar pixels, because reflective and thermal information were complementary. Two-pair images used for the selection ensured that selected similar pixels possessed the same spectral and thermal trajectories. In the computation of the weights for selected similar pixels, the correlation coefficient of the pixel-wise reflective and thermal vector between MODIS and Landsat were utilized to measure the thermal "similarity". The higher similarity would provide a larger weight in the final calculation for the central pixel. With the proposed model SADFAT, it is possible to predict a radiance image using one Landsat reference image, either at time t_1 or t_2. To reduce the uncertainty, the final predicted images in this study were computed based on the two predicted images weighted by the temporal change in radiance at the coarse resolution level.

Another merit of SADFAT is to employ LSMA to address the issue of thermal landscape heterogeneity. This issue is especially important when SADFAT is applied to urban landscapes, where mixed pixels often prevail in medium- or coarse-resolution satellite imagery (Liu & Weng, 2009; Lu & Weng, 2004). To ensure a consistent comparison between MODIS and Landsat data, LST values were first converted to radiances at the Landsat effective thermal wavelength. Then, LSMA linked

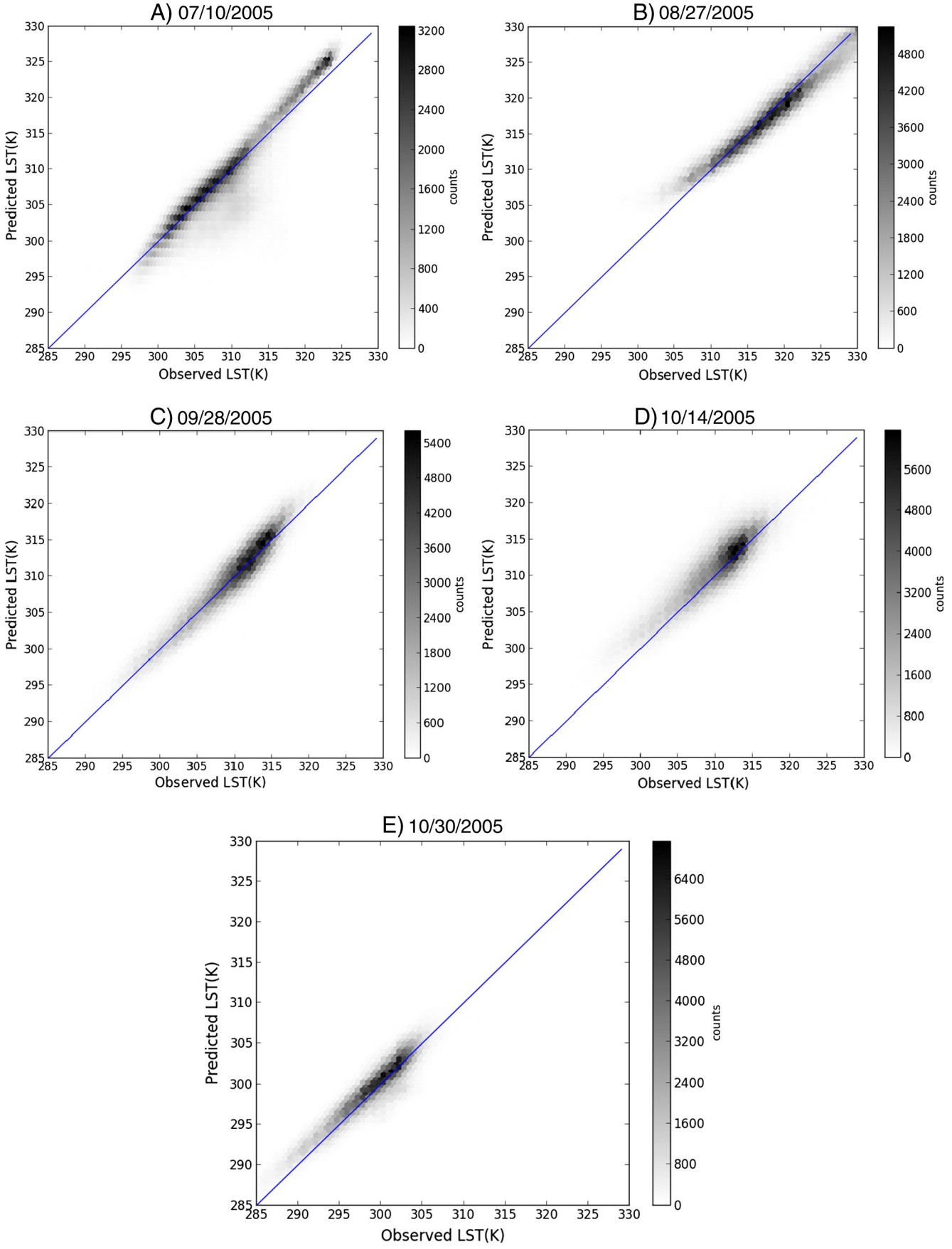

Fig. 5. The scatter plots between the observed and the predicted LSTs on 07/10/2005 (panel A), 08/27/2005 (panel B), 09/28/2005 (panel C), 10/14/2005 (panel D), and 10/30/2005 (panel E).

Table 2
The computed indices of prediction accuracy (unit: K).

Date	Correlation coefficient	Mean difference	Mean absolute difference
07/10/2005	0.96	0.15	1.68
08/27/2005	0.96	−0.47	1.53
09/28/2005	0.95	0.39	1.42
10/14/2005	0.87	1.08	2.03
10/30/2005	0.93	0.48	1.25

the radiation relationship between Landsat and MODIS thermal infrared information. Thus, the temporal change in radiance can be included in the fusion model.

However, it should be noted that SADFAT also contains a few limitations. An assumption for SADFAT was that the phase shift parameter would keep constant. Therefore, SADFAT did not have the ability to predict LST changes that were not reflected in the MODIS and/or Landsat pixels. The use of an ATC model can well approximate the seasonal cycles of LST, but it cannot delineate the specific daily weather and surface conditions that may also affect LST temporal variation, leading to uncertainty in the modeling. Considering the difference in the overpassing time between Landsat-5 and MODIS sensors was small (less than 10 min) for the study area, this study did not correct for the difference in diurnal temperature change between the two sensors. Since their orbital parameters were equal, the viewing (near-nadir) and solar geometries of MODIS were close to those of the corresponding Landsat acquisition (Gao et al., 2006). Nevertheless, the proposed algorithm should be applicable to Landsat-like sensors, such as ASTER, to enhance their temporal frequency, or to any pair of satellite sensors that parallel the relationship between MODIS and Landsat. One important feature of SADFAT is to establish a linkage in radiance change over time between MODIS and Landsat; therefore, as long as radiance changes between paired satellite sensors can be modeled by LSMA and ATC, SADFAT will be practically useful for thermal sharpening, given satellite over-passing, orbital parameters, and viewing geometry being considered. In addition, several parameters must be carefully set, e.g., the window size and the number of land cover classes. Different study areas

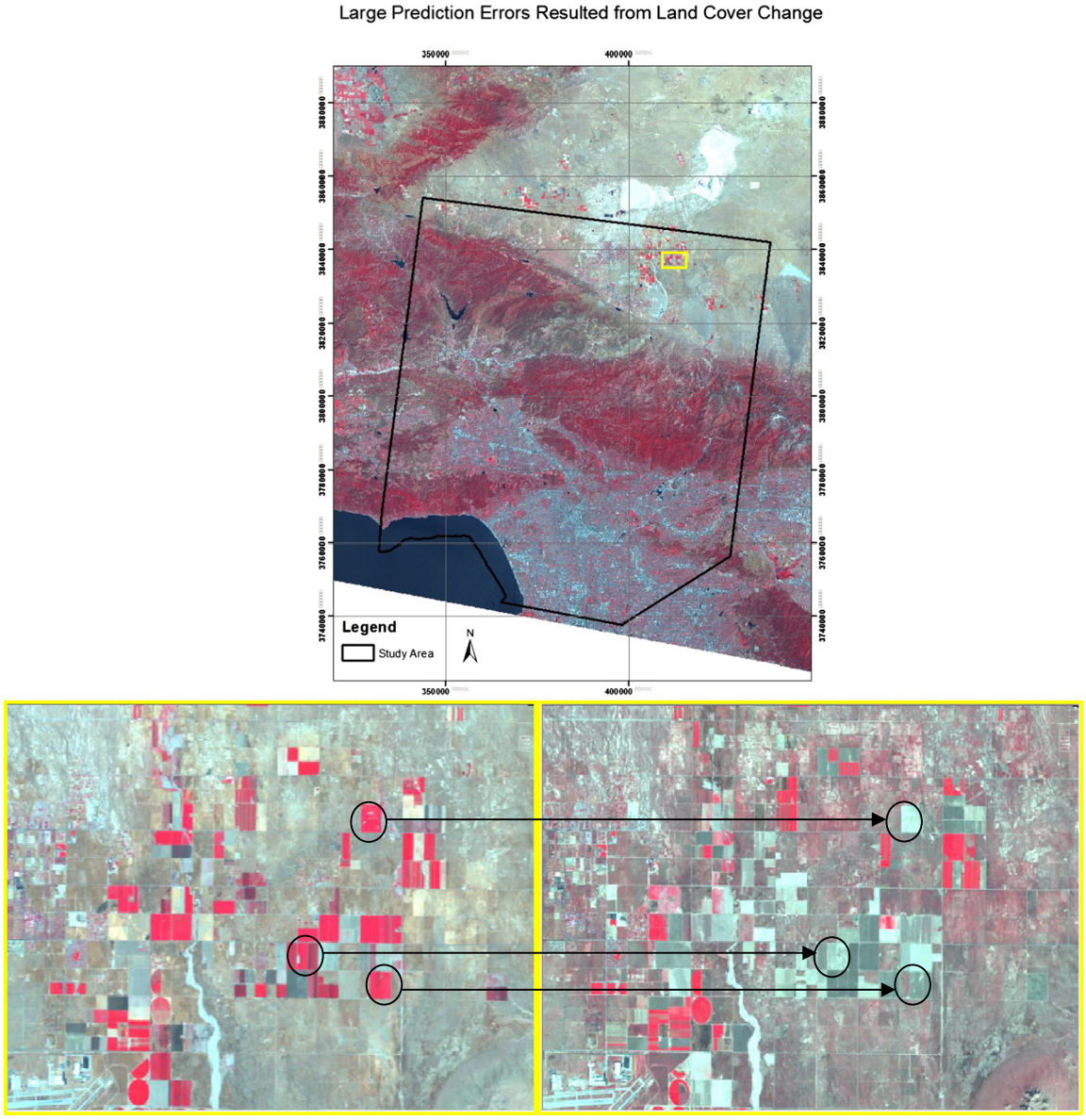

Fig. 6. RGB composite images (R:TM Band 4, G: TM Band 3, B: TM Band 2) on 06/24/2005 (Left) and on 11/15/2005 (Right). Pixels in the circle showed that vegetated areas changed to bare soils over the two reference images. In this condition, prediction errors can be up to 3–5 K.

may require setting up different parameter values, and it is necessary to perform a sensitivity analysis of these parameters before the modeling. The mismatching of Landsat and MODIS pixel was neglected in this study. The variation of MODIS pixel footprint especially at off-nadir viewing may cause some errors and need to be cautioned. Future research is also needed to fill up the missing values caused by clouds. The problem was not so serious in this study since images were carefully selected to avoid cloud contamination. An improved fusion model that can resolve the cloud contamination issue would be useful for areas experiencing more cloudy skies than Los Angeles.

References

Anderson, M. C., Kustas, W. P., Norman, J. M., Hain, C. R., Mecikalski, J. R., & Schultz, L. (2010). Mapping daily evapotranspiration at field to global scales using geostationary and polar orbiting satellite imagery. *Hydrology and Earth System Sciences Discussions*, *7*, 1–34.

Anderson, M. C., Kustas, W. P., Norman, J. M., Hain, C. R., Mecikalski, J. R., Schultz, L., et al. (2011). Mapping daily evapotranspiration at field to continental scales using geostationary and polar orbiting satellite imagery. *Hydrology and Earth System Sciences*, *15*(1), 223–239.

Bechtel, B. (2012). Robustness of annual cycle parameters to characterize the urban thermal landscapes. *IEEE Geoscience and Remote Sensing Letters*, *9*(5), 876–880.

Bechtel, B., Zakšek, K., & Hoshyaripour, G. (2012). Downscaling land surface temperature in an urban area: A case study for Hamburg, Germany. *Remote Sensing*, *4*(10), 3184–3200.

Carlson, T. (2007). An overview of the "triangle method" for estimating surface evapotranspiration and soil moisture from satellite imagery. *Sensors*, *7*(8), 1612–1629.

Dominguez, A., Kleissl, J., Luvall, J. C., & Rickman, D. L. (2011). High-resolution urban thermal sharpener (HUTS). *Remote Sensing of Environment*, *115*(7), 1772–1780.

Gao, F., Masek, J., Schwaller, M., & Hall, F. (2006). On the blending of the Landsat and MODIS surface reflectance: Predicting daily Landsat surface reflectance. *IEEE Transactions on Geoscience and Remote Sensing*, *44*(8), 2207–2218.

Gillespie, A.R. (1992). Spectral mixture analysis of multispectral thermal infrared images. *Remote Sensing of Environment*, *42*(2), 137–145.

Gillies, R. R., Carlson, T. N., Cui, J., Kustas, W. P., & Humes, K. S. (1997). A verification of the 'triangle' method for obtaining surface soil water content and energy fluxes from remote measurements of the Normalized Difference Vegetation Index (NDVI) and surface radiant temperature. *International Journal of Remote Sensing*, *18*(15), 3145–3166.

Gottsche, F. M., & Olesen, F. S. (2001). Modelling of diurnal cycles of brightness temperature extracted from METEOSAT data. *Remote Sensing of Environment*, *76*(3), 337–348.

Hansen, M. C., Roy, D. P., Lindquist, E., Adusei, B., Justice, C. O., & Altstatt, A. (2008). A method for integrating MODIS and Landsat data for systematic monitoring of forest cover and change in the Congo Basin. *Remote Sensing of Environment*, *112*(5), 2495–2513.

Harlan, S. L., Brazel, A. J., Prashad, L., Stefanov, W. L., & Larsen, L. (2006). Neighborhood microclimates and vulnerability to heat stress. *Social Science & Medicine*, *63*(11), 2847–2863.

Hilker, T., Wulder, M.A., Coops, N. C., Linke, J., McDermid, G., Masek, J. G., et al. (2009). A new data fusion model for high spatial- and temporal-resolution mapping of forest disturbance based on Landsat and MODIS. *Remote Sensing of Environment*, *113*(8), 1613–1627.

Hilker, T., Wulder, M.A., Coops, N. C., Seitz, N., White, J. C., Gao, F., et al. (2009). Generation of dense time series synthetic Landsat data through data blending with MODIS using a spatial and temporal adaptive reflectance fusion model. *Remote Sensing of Environment*, *113*(9), 1988–1999.

Huang, P., Wang, J., Song, H., Fu, D., & Wong, F. (2012). Generating high spatiotemporal resolution land surface temperature for urban heat island monitoring. *IEEE Geoscience and Remote Sensing Letters*, *99*. http://dx.doi.org/10.1109/LGRS.2012.2227930.

Hulley, G. C., & Hook, S. J. (2009). The North American ASTER Land Surface Emissivity Database (NAALSED) version 2.0. *Remote Sensing of Environment*, *113*(9), 1967–1975.

Hulley, G. C., Hook, S. J., & Baldridge, A.M. (2008). ASTER land surface emissivity database of California and Nevada. *Geophysical Research Letters*, *35*(13), L13401.

Imhoff, M. L., Zhang, P., Wolfe, R. E., & Bounoua, L. (2010). Remote sensing of the urban heat island effect across biomes in the continental USA. *Remote Sensing of Environment*, *114*(3), 504–513.

Inamdar, A. K., & French, A. (2009). Disaggregation of GOES land surface temperatures using surface emissivity. *Geophysical Research Letters*, *36*(2), L02408. http://dx.doi.org/10.1029/2008GL036544.

Inamdar, A. K., French, A., Hook, S., Vaughan, G., & Luckett, W. (2008). Land surface temperature retrieval at high spatial and temporal resolutions over the southwestern United States. *Journal of Geophysical Research — Atmospheres*, *113*, D07107. http://dx.doi.org/10.1029/2007JD009048.

Jensen, J. R. (2005). *Introductory digital image processing: a remote sensing perspective.*

Jimenez-Munoz, J. C., & Sobrino, J. A. (2003). A generalized single-channel method for retrieving land surface temperature from remote sensing data. *Journal of Geophysical Research — Atmospheres*, *108*(D22), 4688. http://dx.doi.org/10.1029/2003JD003480.

Jin, M. L., Dickinson, R. E., & Zhang, D. L. (2005). The footprint of urban areas on global climate as characterized by MODIS. *Journal of Climate*, *18*(10), 1551–1565.

Kaufman, Y. J., & Gao, B. C. (1992). Remote-sensing of water-vapor in the near IR from Eos/Modis. *IEEE Transactions on Geoscience and Remote Sensing*, *30*(5), 871–884.

Kustas, W. P., Norman, J. M., Anderson, M. C., & French, A. N. (2003). Estimating subpixel surface temperatures and energy fluxes from the vegetation index–radiometric temperature relationship. *Remote Sensing of Environment*, *85*(4), 429–440.

Lafortezza, R., Carrus, G., Sanesi, G., & Davies, C. (2009). Benefits and well-being perceived by people visiting green spaces in periods of heat stress. *Urban Forestry & Urban Greening*, *8*(2), 97–108.

Liu, J. G., & Moore, J. M. (1998). Pixel block intensity modulation: Adding spatial detail to TM band 6 thermal imagery. *International Journal of Remote Sensing*, *19*(13), 2477–2491.

Liu, D. S., & Pu, R. L. (2008). Downscaling thermal infrared radiance for subpixel land surface temperature retrieval. *Sensors*, *8*, 2695–2706.

Liu, H., & Weng, Q. (2009). An examination of the effect of landscape pattern, land surface temperature, and socioeconomic conditions on WNV dissemination in Chicago. *Environmental Monitoring and Assessment*, *159*(1–4), 143–161.

Liu, H., & Weng, Q. (2012). Enhancing temporal resolution of satellite imagery for public health studies: A case study of West Nile Virus outbreak in Los Angeles in 2007. *Remote Sensing of Environment*, *117*, 57–71.

Lu, D. S., & Weng, Q. (2004). Spectral mixture analysis of the urban landscape in Indianapolis with landsat ETM plus imagery. *Photogrammetric Engineering and Remote Sensing*, *70*(9), 1053–1062.

Masek, J. G., Vermote, E. F., Saleous, N. E., Wolfe, R., Hall, F. G., Huemmrich, K. F., et al. (2006). A Landsat surface reflectance dataset for North America, 1990–2000. *IEEE Geoscience and Remote Sensing Letters*, *3*(1), 68–72.

Moran, M. S. (2004). Thermal infrared measurement as an indicator of plant ecosystem health. *Thermal Remote Sensing in Land Surface Processes*, 257–282.

Nichol, J. (1994). A GIS-based approach to microclimate monitoring in Singapore's high-rise housing estates. *Photogrammetric Engineering and Remote Sensing*, *60*(10), 1225–1232.

Nichol, J. (2009). An emissivity modulation method for spatial enhancement of thermal satellite images in urban heat island analysis. *Photogrammetric Engineering and Remote Sensing*, *75*(5), 547–556.

Nicodemus, F. E. (1965). Directional reflectance and emissivity of an opaque surface. *Applied Optics*, *4*(7), 767–773.

Oke, T. R. (1979). *Technical note no. 169: Review of urban climatology*. Geneva, Switzerland: World Meteorological Organization (43 pp.).

Oke, T. R. (1982). The energetic basis of the urban heat island. *Quarterly Journal of the Royal Meteorological Society*, *108*(455), 1–24.

Potapov, P., Hansen, M. C., Stehman, S. V., Loveland, T. R., & Pittman, K. (2008). Combining MODIS and Landsat imagery to estimate and map boreal forest cover loss. *Remote Sensing of Environment*, *112*(9), 3708–3719.

Pu, R. L., Gong, P., Michishita, R., & Sasagawa, T. (2006). Assessment of multi-resolution and multi-sensor data for urban surface temperature retrieval. *Remote Sensing of Environment*, *104*(2), 211–225.

Rajasekar, U., & Weng, Q. H. (2009). Spatio-temporal modelling and analysis of urban heat islands by using Landsat TM and ETM plus imagery. *International Journal of Remote Sensing*, *30*(13), 3531–3548.

Reisen, W., Lothrop, H., Chiles, R., Madon, M., Cossen, C., Woods, L., et al. (2004). West Nile virus in California. *Emerging Infectious Diseases*, *10*(8), 1369–1378.

Ruiz, M.O., Chaves, L. F., Hamer, G. L., Sun, T., Brown, W. M., Walker, E. D., et al. (2010). Local impact of temperature and precipitation on West Nile virus infection in *Culex* species mosquitoes in northeast Illinois, USA. *Parasites & Vectors*, *3*(19).

Sabins, F. F. (1997). *Remote sensing. Principles and interpretation* (3rd ed.). New York: W. H. Freeman & Co.

Sobrino, J. A., Jimenez-Munoz, J. C., & Paolini, L. (2004). Land surface temperature retrieval from LANDSAT TM 5. *Remote Sensing of Environment*, *90*(4), 434–440.

Sobrino, J. A., Jimenez-Munoz, J. C., Soria, G., Romaguera, M., Guanter, L., Moreno, J., et al. (2008). Land surface emissivity retrieval from different VNIR and TIR sensors. *IEEE Transactions on Geoscience and Remote Sensing*, *46*(2), 316–327.

Sobrino, J. A., & Raissouni, N. (2000). Toward remote sensing methods for land cover dynamic monitoring: Application to Morocco. *International Journal of Remote Sensing*, *21*(2), 353–366.

Stathopoulou, M., & Cartalis, C. (2009). Downscaling AVHRR land surface temperatures for improved surface urban heat island intensity estimation. *Remote Sensing of Environment*, *113*(12), 2592–2605.

Streutker, D. R. (2003). Satellite-measured growth of the urban heat island of Houston, Texas. *Remote Sensing of Environment*, *85*(3), 282–289.

Tomlinson, C. J., Chapman, L., Thornes, J. E., & Baker, C. J. (2011). Remote sensing land surface temperature for meteorology and climatology: A review. *Meteorological Applications*, *18*(3), 296–306.

Trenberth, K. E. (1992). *Climate system modeling*. Cambridge, UK: Cambridge University Press.

Weng, Q. (2009). Thermal infrared remote sensing for urban climate and environmental studies: Methods, applications, and trends. *ISPRS Journal of Photogrammetry and Remote Sensing*, *64*(4), 335–344.

Weng, Q., & Fu, P. (2014). Modeling annual parameters of land surface temperature variations and evaluating the impact of cloud cover using time series of Landsat TIR data. *Remote Sensing of Environment*, *140*, 267–278.

Weng, Q., Liu, H., Liang, B. Q., & Lu, D. S. (2008). The spatial variations of urban land surface temperatures: Pertinent factors, zoning effect, and seasonal variability. *IEEE Journal of Selected Topics in Applied Earth Observations and Remote Sensing*, *1*(2), 154–166.

Weng, Q., Lu, D. S., & Schubring, J. (2004). Estimation of land surface temperature–vegetation abundance relationship for urban heat island studies. *Remote Sensing of Environment*, *89*(4), 467–483.

Zakšek, K., & Oštir, K. (2012). Downscaling land surface temperature for urban heat island diurnal cycle analysis. *Remote Sensing of Environment*, *117*, 114–124.

Zhou, Y. Y., Weng, Q., Gurney, K. R., Shuai, Y. M., & Hu, X. F. (2012). Estimation of the relationship between remotely sensed anthropogenic heat discharge and building energy use. *ISPRS Journal of Photogrammetry and Remote Sensing*, *67*, 65–72.

Zhu, X. L., Chen, J., Gao, F., Chen, X. H., & Masek, J. G. (2010). An enhanced spatial and temporal adaptive reflectance fusion model for complex heterogeneous regions. *Remote Sensing of Environment*, *114*(11), 2610–2623.